iScience

Article

Low-intensity pulsed ultrasound-generated singlet oxygen induces telomere damage leading to glioma stem cell awakening from quiescence

Sirong Song, Dongbin Ma, Lixia Xu, Qiong Wang, Lanxiang Liu, Xiaoguang Tong, Hua Yan

hongwu1984teda@126.com (X.T.)
yanhua20042007@sina.com (H.Y.)

Highlights

LIPUS "waked quiescent GSCs up" and enhanced the sensitivity of temozolomide

LIPUS-generated singlet oxygen damaged telomeres, reducing GSCs stemness

Cytochrome B5 and *c* are targets for LIUPS energy transfer

iScience

Article

Low-intensity pulsed ultrasound-generated singlet oxygen induces telomere damage leading to glioma stem cell awakening from quiescence

Sirong Song,[1,5] Dongbin Ma,[1,5] Lixia Xu,[2,5] Qiong Wang,[2] Lanxiang Liu,[3] Xiaoguang Tong,[2,4,*] and Hua Yan[2,4,6,*]

SUMMARY

Cancer stem cells, quiescent and drug resistant, have become a therapeutic target. Unlike high-intensity focused ultrasound directly killing tumor, low-intensity pulsed ultrasound (LIPUS), a new noninvasive physical device, promotes pluripotent stem cell differentiation and is primarily applied in tissue engineering but rarely in oncotherapy. We explored the effect and mechanism of LIPUS on glioma stem cell (GSC) expulsion from quiescence. Here, we observed that LIPUS led to attenuated expression of GSC biomarkers, promoted GSC escape from G0 quiescence, and significantly weakened the Wnt and Hh pathways. Of note, LIPUS transferred sonomechanical energy into cytochrome *c* and B5 proteins, which converted oxygen molecules into singlet oxygen, triggering telomere crisis. The *in vivo* and *in vitro* results confirmed that LIPUS enhanced the GSC sensitivity to temozolomide. These results demonstrated that LIPUS "waked up" GSCs to improve their sensitivity to chemotherapy, and importantly, we confirmed the direct targeted proteins of LIPUS in GSCs.

INTRODUCTION

Cancer stem cells (CSCs) are a special cancer cell population with the capacity of self-renewal, proliferation, and multilineage differentiation, similar to embryonic stem cells (Matteucci et al., 2018; Nusblat et al., 2017). In addition, they exhibit an elevated ability to resist cancer treatment, invasion, immune evasion, and metastasis (Najafi et al., 2019). In contrast to dividing cancer cells with a high metabolism, they generally remain dormant (Clarke et al., 2006). Considering that conventional anticancer therapies have preferentially targeted cells that divide, CSCs are resistant to such treatments, and those CSCs that remain after removal of a large number of cancer cells re-enter the cell cycle after a period of latency, potentially leading to disease recurrence and metastasis. Thus, targeting the transition between quiescence and proliferation in CSCs is a potential strategy to prevent the re-emergence of malignancy.

Gliomas account for approximately 80% of primary malignancies of the central nervous system and have a high mortality rate (Ostrom et al., 2018; Weller et al., 2015). Because of the aggressive growth of gliomas, the prognosis of patients remains extremely poor despite surgery as well as chemotherapy treatment. Glioma stem cells (GSCs) are a subpopulation of glioma cells with the particular ability to proliferate and differentiate. GSCs are considered to play a key role in treatment resistance and tumor recurrence and are a potential therapeutic target for glioma (Hu et al., 2019; Li et al., 2021).

Ultrasound has been widely applied in disease diagnosis (Mayo et al., 2019; Saravelos et al., 2017) and adjuvant therapy (Wang et al., 2017). Low-intensity pulsed ultrasound (LIPUS) has low energy intensity (<3 w/cm^2) and outputs energy in the form of an impulse wave. Owing to its noninvasiveness and few side effects, it has been widely applied in regenerative medicine, such as promoting fracture healing (Harrison et al., 2016), accelerating tissue regeneration (Armstrong et al., 2018), and enhancing thrombolysis (Alexandrov, 2006) and nerve regeneration (Ni et al., 2017). LIPUS could improve the osteogenic differentiation of human mesenchymal stem cells (Costa et al., 2018) and guarantee the maintenance of the osteogenic committed fraction (Armstrong et al., 2018). However, there are few studies about the regulatory effect and the mechanism of LIPUS on GSCs. Based on the role of LIPUS in human mesenchymal stem cells, we hypothesized that LIPUS could "wake up" dormant GSCs to accelerate GSC expulsion from quiescence. The main purpose of our project was to explore whether LIPUS "wakes quiescent GSCs up," decreases their expression

[1]Clinical College of Neurology, Neurosurgery and Neurorehabilitation, Tianjin Medical University, Tianjin 300070, China

[2]Tianjin Neurosurgical Institute, Tianjin Key Laboratory of Cerebrovascular and Neurodegenerative Diseases, Tianjin Huanhu Hospital, Tianjin 300350, P.R.China

[3]Department of Magnetic Resonance Imaging, Qinhuangdao Municipal No. 1 Hospital, No. 258 Wenhua Road, Qinhuangdao 066000, Hebei Province, P.R. China

[4]Department of Neurosurgery, Tianjin Huanhu Hospital, Tianjin 300350, P.R. China

[5]These authors contributed equally

[6]Lead contact

*Correspondence:
hongwu1984teda@126.com
(X.T.),
yanhua20042007@sina.com
(H.Y.)
https://doi.org/10.1016/j.isci.2021.103558

of GSC stem cell-related characteristics, and enhances their sensitivity to chemoradiotherapy to promote the killing role of chemoradiotherapeutic drugs on GSCs to provide new ideas for prolonging the survival of patients.

More interestingly, the mechanism by which ultrasound exerts its energetic effects at the cellular level is still unclear. The CSC energy source relies primarily on mitochondrial respiration, which is distinct from aerobic glycolysis in tumor cells (Garofano et al., 2021; Sharanek et al., 2020). It has been reported that singlet oxygen ($^1O_2$) produced by mitochondria can selectively damage telomeres (Fouquerel et al., 2019; Qian et al., 2019). Telomeres are involved in CSC stemness (Laprade et al., 2020; Rudolph et al., 1999). Accordingly, we explored whether LIPUS produces $^1O_2$ from the mitochondria, leading to a telomere crisis and dysfunction. In addition, as sonosensitizers, cytochrome B5 and c can absorb energy and undergo electronic transitions in response to LIPUS treatment, which are excited from low- to high-energy states, and then transfer the energy to the ground state oxygen molecules to release $^1O_2$.

RESULTS

LIPUS induces differentiation of GSCs

In terms of sphere size, mature GSC spheres comprise greater than 50 cells and have a diameter greater than 50 μm. Ideal GSC spheres have round and smooth edges (Ishiguro et al., 2017; Yu et al., 2008). To investigate the effect of LIPUS on GSCs, GSCs derived from glioblastoma cells were induced *in vitro* and stimulated by LIPUS for 3 consecutive days. The number of mature cell spheres was lower in the LIPUS group than in the control group (Figures 1A and S3A). Under the microscope at 100×, GSC spheres in the LIPUS group were smaller and uneven in size, with loose cells and less tight intercellular connections than those of the control group (Figure 1A), indicating that LIPUS changed the morphology of the tumor spheroids, triggering the production of GSC spheres with protrusions such as are found in tumor cells, and promoted the GSCs to move from a stem cell state to a nonstem cell state.

Next, we used immunofluorescence staining and flow cytometry to detect changes in the expression levels of the stem cell surface markers, including CD133 and Nestin protein (Figures 1B and S3B). Immunofluorescence results showed that CD133 and Nestin fluorescence signals were significantly weaker in the LIPUS group than in the control group. The flow cytometry results of Nestin also corroborated these results (Figure 1C). The quantitative transcription-polymerase chain reaction (qPCR) results showed that the gene expression levels of the stem-related transcription factors Nanog, Oct4, and Sox2 and the stem cell markers CD133 and Nestin after LIPUS intervention at different times were all lower than those of the control group (Figures 1D and S3C). These results suggest that LIPUS induces the loss of stem cell-related characteristics and the differentiation of GSCs.

LIPUS regulates the G2/M checkpoint and reduces stem cell characteristics of GSC

We used BrdU flow cytometry to investigate whether LIPUS is associated with the regulation of the GSC cell cycle (Figure 2A). GSCs arrest in a quiescent G0 phase. Compared with the control group, G0/G1 cells were less abundant and the number of G2/M cells was approximately doubled in the LIPUS group. These results suggest that LIPUS "woke up" dormant GSCs from the quiescent G0 phase into the active G2/M phase, inducing GSC differentiation. We then further clarify the role of LIPUS on the key proteins of the G2/M checkpoint, including PLK1, CDK1, and Cyclin B. The western blot results showed that the expression levels of PLK1, CDK1, and Cyclin B increased significantly after LIPUS treatment (Figures 2B and S3D). These results suggest that LIPUS promoted the mitosis of GSCs from the G0 phase to the G2/M phase.

LIPUS inhibits the Hh/Wnt pathway and reduces the stem cell-related characteristics of CSCs

The self-renewal and stemness maintenance of CSCs are regulated by a variety of signaling pathways, and the Hedgehog (Hh) and Wnt/β-catenin pathways are well known. To determine how LIPUS reduced GSC stemness, we found by western blot (Figures 2C and S3D) that the expression levels of Wnt3, Wnt5a, and β-catenin, the key nodes of Wnt signaling, were reduced by more than half. Similarly, the expression levels of Gli1 and PTCH, the key nodes of the Hh signaling pathway, were significantly reduced. These results indicated that LIPUS inhibited the Hh/Wnt pathway to reduce GSC stem cell-related characteristics.
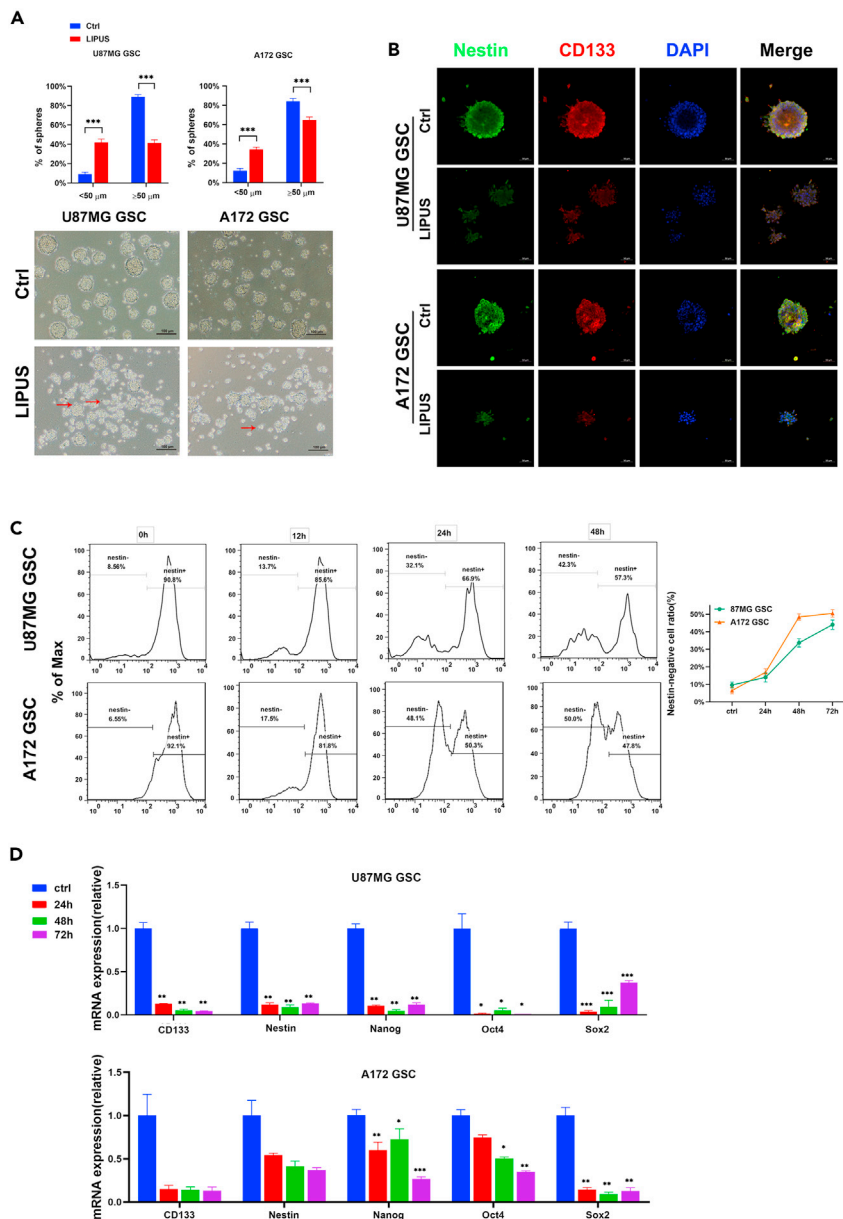
Figure 1. LIPUS induces differentiation of GSCs

(A) GSC sphere formation ratio with LIPUS treatment. Red arrows indicate GSC spheres with extended antennae. n = 6.

(B) Images of GSC spheres that expressed stem cell markers Nestin (green) and CD133 (red) by immunofluorescence. DAPI (blue) for nuclei.

(C) Nestin expression levels in GSC with LIPUS treatment in 24, 48, and 72 h and Nestin-negative cell ratio by flow cytometry. n = 3.

(D) qPCR analysis of mRNA expressions in GSCs with LIPUS treatment in 24, 48, and 72 h, respectively. n = 3. $*p \leq 0.05$, $**p \leq 0.01$, $***p \leq 0.001$.

LIPUS shortens the telomere length and leads to telomere damage

We detected telomere length and integrity in GSCs after LIPUS treatment by quantitative polymerase chain reaction (qPCR), metaphase spread, and telomere fluorescence *in situ* hybridization (FISH). Compared with the control group, The telomere length (T/S) in the LIPUS group was shorter. Moreover, T/S in the LIPUS group of U87MG GSC was three-quarters that in the control group (Figures 3A and S3E). The fluorescence intensity of the telomeres in the LIPUS group was significantly weaker. The results of the metaphase spread
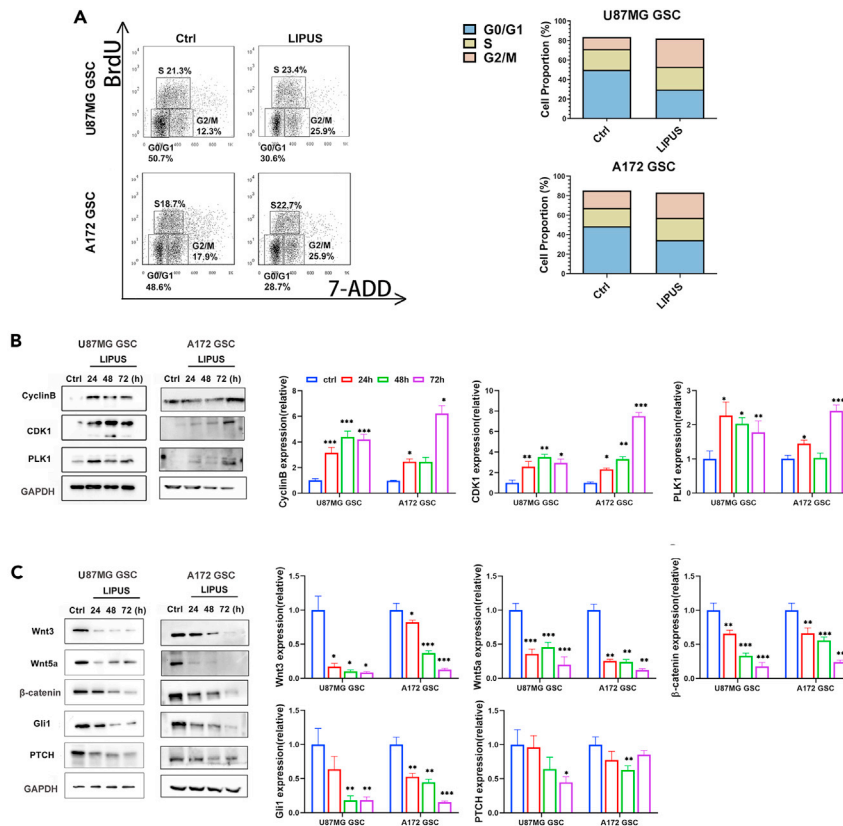
Figure 2. LIPUS regulates the G2/M checkpoint and reduces stem cell characteristics of GSC

(A) The BrdU and 7-AAD analysis of GSCs with LIPUS treatment by flow cytometry, n = 3.

(B) Western blotting analysis expression of the key proteins of the G2/M checkpoint. The results represent ratios of each protein and GAPDH levels and are normalized to Ctrl.

(C) Western blotting analysis expression of the key nodes of the Hedgehog (Hh) and Wnt/β-catenin pathways. The results represent ratios of each protein and GAPDH levels and are normalized to Ctrl. $*p \leq 0.05$, $**p \leq 0.01$, $***p \leq 0.001$.

and telomere FISH showed that there were abnormal telomere signals, including multiple telomeric signals and telomere signal-free ends. The results of the metaphase spread and telomere FISH showed that the median number of abnormal telomere signals in each cell of the control group was two, whereas it was six per cell in the LIPUS group, suggesting telomere length shortening and telomere loss due to LIPUS treatment (Figure 3B).

53 bp1 is a DNA repair protein of double-stranded breaks, which is known to be recruited to telomeres upon double-stranded break formation (Fouquerel et al., 2019; Varela et al., 2016). We explored whether there was telomere damage in GSCs by immunofluorescence and telomere fluorescence *in situ* hybridization (IF-FISH) technology (Figure 3C). Telomere dysfunction-induced foci (TIFs) where telomeres and the 53 bp1 fluorescence signal colocalize indicate telomere damage. There were more fluorescence signal points of TIFs in the LIPUS group, with an average of 3.8 TIFs per cell and 0.57 TIFs per cell in the control group. The number of TIFs in the LIUPS group was significantly higher than that in the control group, indicating that LIPUS caused telomere damage and inhibited the DNA protection function of telomeres.

LIPUS on mitochondrial cytochrome produces $^1O_2$, inducing telomere injury

In healthy cells, where the mitochondrial membrane potential is high, JC-1 forms complexes known as J-aggregates, which display intense red fluorescence. However, in depolarized cells, JC-1 is still present as a monomer, showing green fluorescence (Nechiporuk et al., 2019). The ratio of red/green fluorescence intensity was used to reflect the mitochondrial membrane potential. First, we monitored changes in the mitochondrial membrane potential. The results showed that the red/green fluorescence intensity ratio in the LIPUS group was significantly lower than that in the control group, suggesting that the mitochondrial
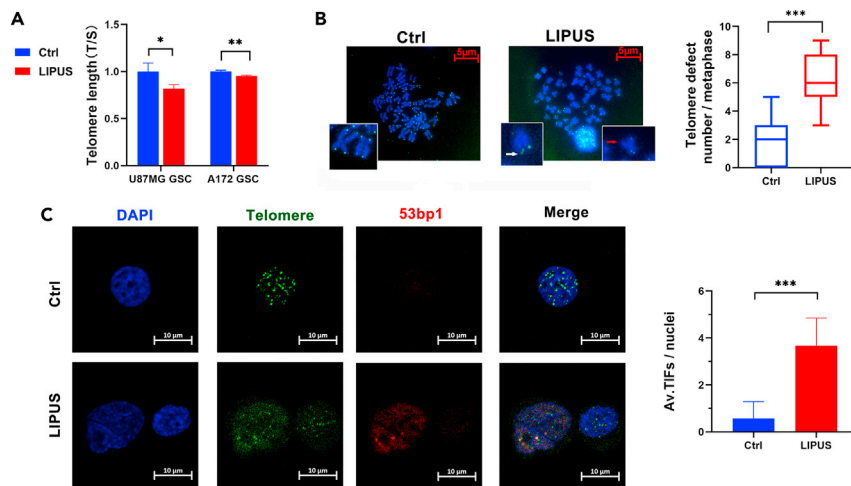
Figure 3. LIPUS shortens the telomere length and leads to telomere damage

(A) qPCR analysis of the telomere length (T/S) in GSCs with LIPUS treatment. n = 3.

(B) Telomere metaphase spread and telomere fluorescence *in situ* hybridization analysis in GSCs with LIPUS treatment (red arrow indicates telomeric loss and white arrow indicates fragile telomeres). Quantification of incomplete telomere. Each dot for a metaphase. Medians (bar) from three independent experiments (n = 30 for each experiment).

(C) Telomere fluorescence *in situ* hybridization of TIFs in GSCs with LIPUS treatment (red for 53 bp1 and green for telomeres). Quantification of the average (av.) number of TIFs per nuclei. n = 3, at least 30 cells per experiment. *$p \leq 0.05$, **$p \leq 0.01$, ***$p \leq 0.001$.

membrane potential decreased significantly with LIPUS treatment (Figures 4A and S3F). Thus, LIPUS caused mitochondrial damage and oxidative stress. At 24, 48, and 72 h after stimulation by LIPUS, the ratio of red/green fluorescence intensity decreased successively (Figure 4B), indicating that the influence of LIPUS on the mitochondrial membrane potential was positively correlated with the stimulation duration.

It has been reported that $^1O_2$ produced by mitochondria can damage telomeres in a targeted manner (Fouquerel et al., 2019; Qian et al., 2019). Therefore, we used a singlet oxygen detection kit to detect the influence of LIPUS on $^1O_2$ production in GSCs (Figures 4C, 4D, and S3G). The results showed that the fluorescence intensity of probe R in the LIPUS group was higher than that in the control group, indicating that the level of $^1O_2$ in the LIPUS group was higher than that in the control group. This suggests that LIPUS increased $^1O_2$ production in GSCs.

To further clarify the mechanism of the effect of LIPUS on $^1O_2$, we conducted *in vitro* experiments. We detected $^1O_2$ production in pure proteins of recombinant cytochrome B5a (cyt B5a), cytochrome B5b (cyt B5b), cytochrome *c* (cyt *c*) and cytochrome *c*1 (cyt *c*1) after LIPUS treatment. The results showed that the standard fluorescence intensity of probe R in the cyt B5 group was significantly higher than that in the control group, indicating that $^1O_2$ production in the LIPUS group was higher than that in the control group (Figure 4E). In the cyt *c* group, the standard fluorescence intensity of probe R was higher than that of the control group (Figure 4F), indicating that the $^1O_2$ production in the LIPU group was higher than that of the control group. These results suggest that LIPUS produces $^1O_2$ by acting on the cyt B5 family and cyt *c* family to trigger intracellular oxidative stress.

Mito-TEMPO recovered the stemness of the LIPUS-suppressed GSCs

Mito-TEMPO is a mitochondria-targeted superoxide dismutase with the ability to scavenge superoxide and alkyl radicals (Wei et al., 2020). We used a singlet oxygen scavenger to clarify that LIPUS-generated $^1O_2$ reduced the stem cell characteristics of GSCs. Low-level mito-TEMPO has limited effect on the growth of GSCs (Figure S4). First, we demonstrated that mito-TEMPO reduces cellular singlet oxygen levels (Figures 5A and 5B). Then, to observe the inhibitory effect of $^1O_2$ on the GSC stem cell properties, we observed the GSC sphere-forming capacity and the expression levels of stem cell-related factors with mito-TEMPO treatment. We found a restoration of LIPUS-treated GSC sphere-forming ability with mito-TEMPO treatment (Figure 5C). The flow cytometry results also showed that, compared with the LIPUS group, the
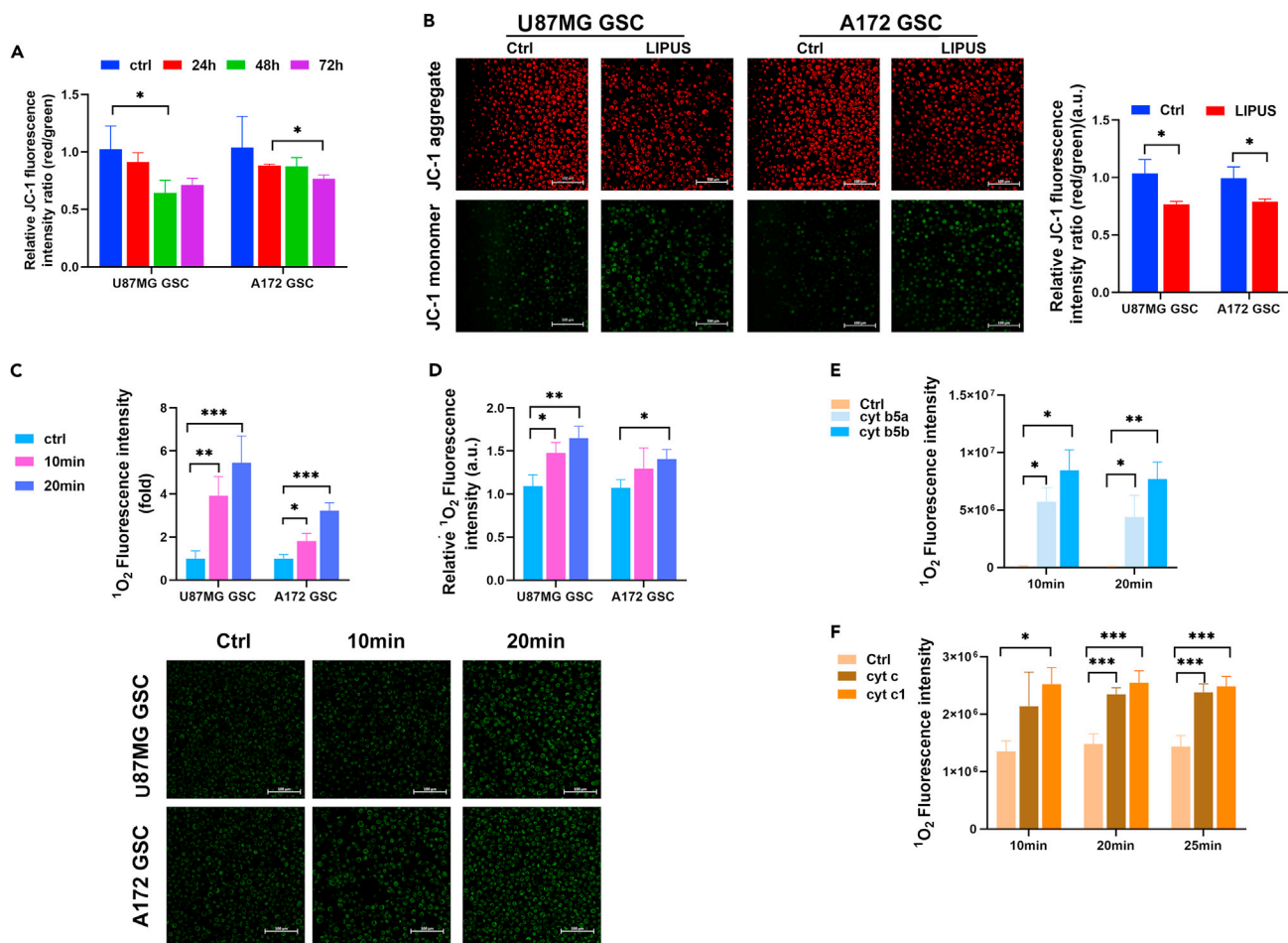
Figure 4. LIPUS on mitochondrial cytochrome (cyt) generates singlet oxygen ($^1O_2$)

(A) JC-1 fluorescence intensity of GSCs with LIPUS treatment by the microplate reader. n = 3.

(B) Mitochondrial membrane potential analysis of GSCs with LIPUS treatment. The results of quantified fluorescence images are normalized to Ctrl. n = 3.

(C) $^1O_2$ generation in GSCs with LIPUS treatment for 10 and 20 min. The results of quantified fluorescence images are normalized to Ctrl. n = 3.

(D) $^1O_2$ generation analysis in GSCs by the microplate reader. n = 3.

(E and F) $^1O_2$ generation analysis in recombinant cyt with LIPUS treatment for 10 and 20 min, respectively, by the microplate reader. n = 3. $*p \leq 0.05$, $**p \leq 0.01$, $***p \leq 0.001$.

proportion of nestin-positive GSCs of the LIPUS &mito-TEMPO group significantly increased (Figure 5D). There was little difference between the mito-TEMPO group and LIPUS&mito-TEMPO group of most of stem cell-related factors expression levels by qPCR (Figure 5E-F), which means that mito-TEMPO interrupted the effect of $^1O_2$ produced by LIPUS on GSCs. Under confocal microscopy, the fluorescence signals of CD133 and nestin of the mito-TEMPO were same as the LIPUS&mito-TEMPO group (Figure S5). These results indicate that mito-TEMPO reversed some effect of LIPUS on the inhibition of GSC stemness.

Of note, LIPUS induced telomere damage. Telomeres in the LIPUS&mito-TEMPO group were longer than those in the LIPUS group and were not significantly different from those in the control group (Figure 5G). The results of the mitochondrial membrane potential assay were similar. The red/green fluorescence intensity ratio was higher in the LIPUS&mito-TEMPO group than in the LIPUS group of A172 GSCs (Figures 5H and 5I). This suggests that mito-TEMPO reduced the damage to telomeres caused by $^1O_2$ produced by LIPUS.

LIPUS enhances the chemotherapeutic sensitivity of temozolomide and increases the cytotoxic effect on GSCs

As CSCs are closely linked to tumorigenicity and chemoresistance, the definitive eradication of CSCs is of great clinical value. Compared with the temozolomide (TMZ) group (500 μM TMZ, Figure S6), the
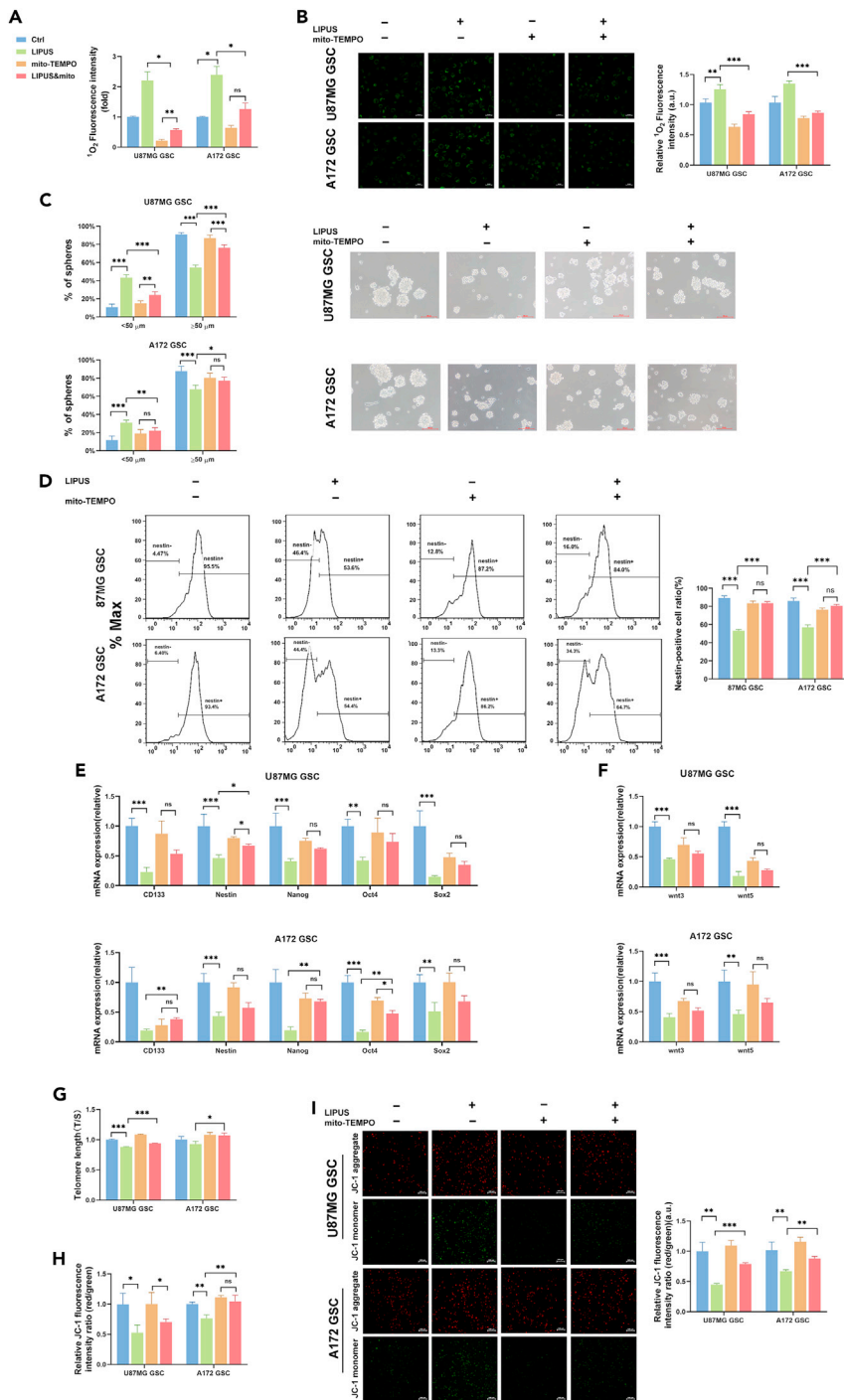
Figure 5. Mito-TEMPO rescued the suppressive effect of LIPUS on GSC stem cell properties

(A) MitoTEMPO (5 μM) inhibited mitochondrial $^1O_2$ generation after LIPUS treatment. $^1O_2$ generation analysis in GSCs 24 h after treatment with LIPUS and mito-TEMPO (5 μM) using the microplate reader. n = 3.

(B) $^1O_2$ generation in GSCs. The results of quantified fluorescence images are normalized to Ctrl. n = 3.

(C) The GSC sphere formation ratio, showing the ability of sphere formation. n = 3.

(D) Nestin expression levels in GSC and Nestin-negative cell ratio by flow cytometry. n = 3.

(E and F) qPCR analysis of mRNA expression of stem-related transcription factors and the key nodes of Wnt signaling in GSCs after treatment with LIPUS and mito-TEMPO (5 μM). n = 3.

Figure 5. *Continued*

(G) qPCR analysis of the telomere length (T/S) in GSCs. n = 3.

(H) JC-1 fluorescence intensity of GSCs with LIPUS treatment and mito-TEMPO (5 μM) by the microplate reader. n = 3.

(I) Mitochondrial membrane potential analysis of GSCs with LIPUS treatment and mito-TEMPO (5 μM). The results of quantified fluorescence images are normalized to Ctrl. n = 3. *$p \leq 0.05$, **$p \leq 0.01$, ***$p \leq 0.001$.

proportion of GSC apoptotic cells in the LIPUS&TMZ group was higher (28% versus 17%) in the Annexin V-APC/7-aminoactinomycin D (7-AAD) assay, suggesting that LIPUS enhanced the cytotoxic effect of TMZ on GSCs (Figure 6A).

To investigate the effect of LIPUS on tumor resistance to chemotherapy, we constructed a nude mouse model of subcutaneous implantation (Figure 6B). Twenty nude mice were randomly divided into four groups: Ctrl, LIPUS, TMZ, and LIPUS&TMZ. After 7 days of tumor implantation, the mice began to receive LIPUS and TMZ treatment (60 mg/kg/day via intra-peritoneal injection for 5 consecutive days) (Han et al., 2020). The size of the tumor changed obviously on the eighth day. As shown in Figure 6B, the tumor volume of the LIPUS&TMZ group was significantly smaller than that of the other groups on the 16th day of treatment. The tumor volume of the control group was nearly 3.75 times that of the LIPUS&TMZ group, suggesting that LIPUS&TMZ significantly inhibited tumor growth. The tumor volume of the TMZ group was almost 1.5 times that of the TMZ&LIPUS group, illustrating that LIPUS enhanced the cytotoxic effect of TMZ and had a negative impact on tumor growth in combination with TMZ.

To thoroughly investigate the effect of LIPUS combined with TMZ on tumor cell growth, tumor tissues were fixed and sectioned for TdT-mediated dUTP nick end labeling (TUNEL) and Ki67 staining at the end of the 16-day experimental period to analyze the apoptosis and proliferation of tumor tissues, respectively. The TUNEL results showed that, on average, there were two positive cells in each field of vision in the control group, 4.75 in the LIPUS group, 14.75 in the TMZ group, and 21.75 in the LIPUS&TMZ group (Figure 6C). The Ki-67 results showed that, in the control group, the level of Ki-67 expression was the highest, and the positive area accounted for 90% in each field of vision, 62% in the LIPUS group, 35% in the TMZ group, and 15% in the LIPUS&TMZ group (Figure 6D). Compared with that in the control group, the tumor size in the LIPUS group was smaller, with higher expression of TUNEL and lower expression of Ki67, suggesting that LIPUS inhibited the growth of tumors *in vivo*. Compared with the TMZ group, there was a decrease in the tumor size and the expression of Ki67 and an increase in the expression of TUNEL in the LIPUS&TMZ group, indicating that LIPUS enhanced the chemotherapy sensitivity of glioma to TMZ.

qPCR results showed CD133 and Nestin expression was weaker both in the LIPUS and LIPUS&TMZ (Figures 6E and 6F) groups, which suggested that LIPUS reduced the resistance of CSCs to chemotherapeutic agents and promoted CSC differentiation.

DISCUSSION

CSCs, closely related to tumor invasion, metastasis, and chemoradiotherapy tolerance (Clarke et al., 2006; Zhou et al., 2009), have become an important therapeutic target (Auffinger et al., 2014; Saygin et al., 2019). As a novel noninvasive physical device, sonodynamic therapy can reversibly break the blood-brain barrier, boosting the delivery of drugs to the brain and effectively killing tumors (Guzman et al., 2005; Ting et al., 2012). In contrast to the strong cytotoxicity of high-intensity focused ultrasound on tumors, LIPUS has been reported to promote myoblast alignment for tissue engineering and the differentiation of mesenchymal stem cells in the treatment of spinal cord injury (Costa et al., 2018; Ning et al., 2019).

Compared with tumor cells, CSCs are more sensitive to sonication interventions (Xu et al., 2012). There are few reports about the effect of LIPUS on the stemness of CSCs. This study is the first to explore LIPUS to promote GSC differentiation and reverse GSC chemoresistance, providing a new idea for clinical treatment. Moreover, this study explored the energy conversion of LIPUS in cells without adding acoustic sensitizers, making it clear that LIPUS acts on the intracellular cytochrome family.

CSCs, mostly in the G0 phase of the cell cycle, remain quiescent for a long time with a very low metabolism. DNA replication, transcription, and translation are almost suspended. Therefore, conventional chemotherapeutic agents targeting dividing cells cannot eliminate them, even though CSCs are in small quantities and have inadequate proliferation (Matteucci et al., 2018; Reya et al., 2001). CSCs have strong DNA repair ability with active telomerase and drug resistance and are regulated by a series of signaling pathways, such
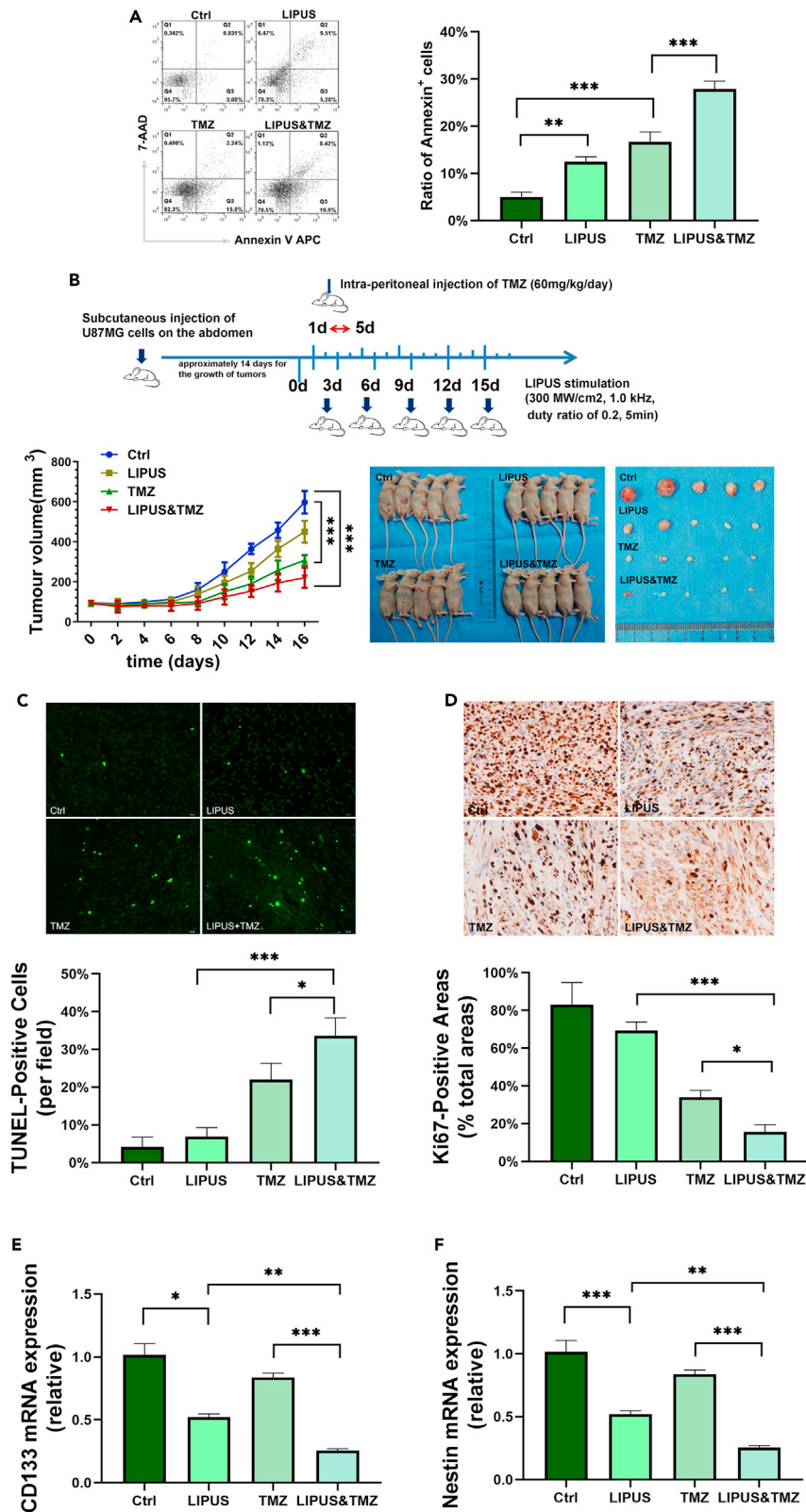
Figure 6. LIPUS enhances the chemotherapeutic sensitivity of TMZ and increases the cytotoxic effect on GSCs

(A) Annexin V-APC/7-AAD assay of GSCs with LIPUS treatment and TMZ (500 μM) by flow cytometry. n = 3.

(B) Treatment of mice with TMZ (60 mg/kg/day via intra-peritoneal injection for 5 consecutive days) and LIPUS (once every 3 days, 300 MW/cm^2, 1.0 kHz). The longest diameter (A) and the shortest diameter (B) of the tumor nodules measured with Vernier calipers daily. The tumor volume was calculated according to the formula V = 1/6π (ab^2).

(C) TUNEL assay for the apoptosis level of tumor tissues.

(D) Ki67 assay for the proliferation level of tumor tissues.

(E and F) qPCR analysis of mRNA expression of stem cell markers. n = 3. *$p \leq 0.05$, **$p \leq 0.01$, ***$p \leq 0.001$.

as the Wnt pathway, Notch pathway, and Hedgehog (Hh) pathway (Mizuno et al., 2010; Wang et al., 2018). In this experiment, the wnt pathway and the Hh pathway were suppressed. In addition, the gene expression levels of the stem cell-related transcription factors Nanog, Oct4, and Sox2 and the stem cell markers CD133 and Nestin were decreased.

In contrast to the adherent growth of most tumor cells, CSCs have a tendency to form tumor spheres in suspension (Ishiguro et al., 2017). Mature CSC spheroids are round and smooth. After LIPUS treatment, the sphere-forming ability of the GSCs was significantly affected. In particular, the cells around the GSC spheroids extended their tentacles and changed from round cells to narrow cells, similar to tumor cells. These results suggest that LIPUS inhibits the maintenance of GSC stem cell-related characteristics. The cell cycle result showed that the key proteins at the G2/M checkpoint were significantly upregulated and that the cell ratio in the G2/M phase was obviously increased in response to LIPUS treatment. This indicates that LIPUS promotes quiescent GSCs to transition from the G0 phase to the G2/M phase to prepare proteins and other substances for mitosis.

Current chemoradiotherapy mainly targets tumor cells in the proliferative phase and plays a killing role during tumor cell division. However, chemoradiotherapy cannot kill GSCs because DNA replication stops in the G0 phase. Then, we speculated that LIPUS-treated GSCs would reduce chemoradiotherapy resistance and that it could increase treatment efficacy. Our results showed that, in LIPUS-treated GSCs, the stem cell characteristics became less obvious, whereas the sensitivity to the chemotherapy drug TMZ was increased and the drug resistance was reduced. These results suggested that, compared with TMZ treatment, the volume of the tumors in response to LIPUS&TMZ treatment was diminished. Meanwhile, the results of TUNEL and Ki67 staining also suggested that LIPUS enhanced the cytotoxicity of TMZ, promoted the apoptosis of tumor cells, and inhibited the proliferation of tumor cells. It is clear that LIPUS promoted the inhibitory effect of TMZ on the biological activity of tumor cells and enhanced the sensitivity of subcutaneous U87MG-transplanted tumors to TMZ *in vivo* (Wu et al., 2019). LIPUS, as a physical means, can provide new ideas for clinical solutions to postoperative chemotherapy drug resistance, improve the efficacy of chemotherapy drugs, and reduce tumor recurrence (Qu et al., 2020; Trendowski et al., 2015; Wan et al., 2019).

The metabolic characteristics of CSCs are distinct from those of proliferating tumors. Proliferating tumor cells rely on aerobic glycolysis, known as the Warburg effect, whereas CSCs with a slow cycle are likely to prefer mitochondrial respiration as their main energy source (Garofano et al., 2021; Sharanek et al., 2020).The parameters we used for ultrasound were diagnostic ultrasound parameters with few side effects on normal cells. This is the basis on which the findings of this study can be applied to clinical treatment. LIPUS induced depolarization of the mitochondrial membrane potential and mitochondrial apoptosis and promoted oxidative stress. As the "energy factory" of cells, mitochondria are damaged and disrupted, producing a large amount of reactive oxygen species (ROS), which induces DNA and telomere damage (Liu et al., 2009; Passos et al., 2007). Persistent DNA damage could aggravate mitochondrial disorders and release more ROS (Vousden and Lane, 2007), thus inducing grave DNA damage.

Moreover, it is difficult for telomeres to be repaired during regular DNA repair (Ozer et al., 2018; Ozer and Hickson, 2018). Telomeres are the "caps" that adorn the ends of human chromosomes and are composed of TTAGGG repeated sequences. Telomeres are mainly involved in DNA repair, protect the ends of chromosomes, delay chromosome shortening, and maintain chromosome stability (Laprade et al., 2020; Mendez-Bermudez et al., 2020; Tarry-Adkins et al., 2008). In addition, telomerase activity is upregulated to maintain proliferation and self-renewal in germ cells and embryonic stem cells. Active telomerase is also one of the characteristics of CSCs (Varela et al., 2016). The FISH and q-PCR results suggested that telomere length was significantly shortened and telomere deletion increased in response to LIPUS treatment. 53 bp1

is recruited to telomeres in response to the double-stranded break formation and acts as a DNA repair protein. The IF-FISH results suggested that the number of 53 bp1-positive TIFs increased significantly after LIPUS, indicating a telomere crisis. Elise Fouquerel et al. reported that local singlet oxygen ($^1O_2$), a type of ROS, specifically induces guanine (G) on telomeres to produce 8-oxoG, causing telomere damage (Fouquerel et al., 2019; Qian et al., 2019). Moreover, 8-oxoG reduces DNA polymerase and telomerase activity, shortening telomeres. Our results indicated that with LIPUS treatment, $^1O_2$ production in GSCs was significantly increased, and the telomeres were destroyed. Therefore, we found that LIPUS is related to telomere damage by $^1O_2$, the mechanism by which LIPUS inhibits the stemness expression of CSCs and promotes CSC expulsion from quiescence.

Most of the current studies on sonodynamic therapy combine synthetic acoustic sensitizers. There are no detailed studies on whether these acoustic sensitizers have any harmful effects on human health or whether they can be used for clinical treatment. This experiment found targets in the cells that can transfer energy from LIPUS. Sonosensitizers in tumor cells, such as hematoporphyrin, absorb energy and undergo electronic transitions after ultrasonic treatment, where they are excited from a low-energy state to a high-energy state, then transfer their energy to the ground-state oxygen molecules to release $^1O_2$ and cause irreversible damage to cancer cells (Zhang et al., 2018). Ma et al. successfully synthesized three metal 4-methylphenylporphyrin complexes and encapsulated them with human serum albumin to form novel nanosonosensitizers (Ma et al., 2019). These nanosonosensitizers generated abundant $^1O_2$ in response to ultrasonic irradiation. Cytochrome (cyt) has excellent absorption properties for visible light owing to its iron-containing heme prosthetic group. In human somatic cells, cytochromes widely exist in organelles and the cytoplasmic matrix. Among them, cyt $c1$ and cyt c both contain one heme, which is distributed in the inner mitochondrial membrane and is higher in metabolically active cells (Daijima and Komatsu, 2014).

Studies have shown that glioma cells have calcium overload and significantly increased ROS after ultrasound treatment. It is believed that the endoplasmic reticulum may be the main target of hemoporphyrin monomethyl ether-sonodynamic therapy (Li et al., 2011). Cyt B5a and cyt B5b both contain one heme and are distributed in the endoplasmic reticulum and mitochondria. Therefore, we suspect that LIPUS, as a form of physical energy, causes the heme prosthetic groups of the cyt c family and cyt B5 family in mitochondria to undergo an electronic transition to produce $^1O_2$. We found that LIPUS significantly elevated $^1O_2$ production *in vitro* in response to LIPUS stimulation of recombinant cyt c, cyt $c1$, cyt B5a, and cyt B5b proteins, again confirming that the mitochondrial respiratory chain members cyt c, cyt $c1$, cyt B5a, and cyt B5b may be the targets for LIPUS energy conversion. We propose that cytochromes should be able to produce $^1O_2$ with different efficiencies under ultrasound irradiation. In future studies, we will compare the efficiency of $^1O_2$ generation by the cyt c family and cyt B5 family.

The previous literature generally believed that ultrasound induced sonosensitizers to produce $^1O_2$ owing to acoustic cavitation and sonoluminescence (Dezhkunov et al., 2000, 2018; Sazgarnia et al., 2013), but this often requires a higher sound intensity beyond diagnostic dose ultrasound. Ultrasound, as a kind of material vibration wave, can form phonons at the level of protein macromolecules and cause phonon-electron coupling (Viani et al., 2014). Phonons change sonosensitizers from the ground state to the excited state, and then the excited sonosensitizers can convert triplet oxygen molecules (the main form of oxygen molecules in the air) into singlet states. Therefore, we believe that acoustic cavitation and sonoluminescence may not be its internal mechanism but instead that LIPUS causes phonon-electron coupling in protein macromolecules to induce electronic transitions and then improve $^1O_2$ generation. Currently, there are few results available to prove this viewpoint in this project. We will confirm it in future research.

Currently, most researchers focus on the killing effect of ultrasound on tumors, whereas our experiment focused on the "waking up" effect of LIPUS on CSCs. In contrast to studies on sonodynamic therapy combined with synthetic sonosensitive agents, we found that the cyt B5 and cyt c families with LIPUS and mitochondria increased intracellular $^1O_2$ production through energy transfer and electron transitions rather than through adding exogenous sonosensitive agents. $^1O_2$ induces telomere damage, shortens telomeres, and promotes the differentiation of dormant CSCs into metabolically active tumor cells.

In summary, LIPUS awakens quiescent GSCs, enhances the cytotoxic effects of TMZ and increases TMZ sensitivity. It provides a new way to solve the problem of postoperative chemoradiotherapeutic drug tolerance in patients with clinical glioma and avoids the damage to normal brain tissue caused by high field

intensity ultrasound due to high energy and scattering. Based on abundant experience in the application of low-field intensity ultrasound in clinical diagnosis (Mayo et al., 2019), such as color Doppler ultrasonography for pregnant women, the biosafety of this energy range has been fully affirmed (Saravelos et al., 2017), which also provides reference experiences and application prospects for the treatment of "tumor stem cell wake-up" by repeated low-field intensity ultrasound.

Limitations of the study

We used subcutaneous tumor models instead of intracranial orthotopic models because of the limitations of the experimental platform. LIPUS travels through the skull with energy loss and could transiently and reversibly open the blood-brain barrier. Further intracranial orthotopic model is considered to replicate the clinical situation accurately.

STAR★METHODS

Detailed methods are provided in the online version of this paper and include the following:

- KEY RESOURCES TABLE
- RESOURCE AVAILABILITY
  - Lead contact
  - Materials availability
  - Data and code availability
- EXPERIMENTAL MODEL AND SUBJECT DETAILS
  - Cell culture and dedifferentiation
  - Tumor xenograft study
  - LIPUS stimulating
- METHOD DETAILS
  - Immunofluorescence staining
  - CCK-8 assay
  - Annexin V/7-AAD apoptosis assay
  - 5-Bromodeoxyuridine (BrdU)
  - Fluorescence-activated cell sorting (FACS)
  - qPCR (quantitative PCR) and RT-PCR (reverse Transcription-PCR)
  - Metaphase spreads and telomere fluorescence in situ hybridization (FISH) analysis
  - Immunofluorescence and telomere fluorescence *in situ* hybridization (IF-FISH)
  - Western blotting
  - Mitochondrial membrane potential assay
  - Singlet oxygen ($^1O_2$) detection
  - Immunohistochemistry
- QUANTIFICATION AND STATISTICAL ANALYSIS

SUPPLEMENTAL INFORMATION

Supplemental information can be found online at https://doi.org/10.1016/j.isci.2021.103558.

AUTHOR CONTRIBUTIONS

Conceptualization, H.Y. and X.T.; methodology, S.S., D.M., and L.X.; investigation, S.S., D.M., and L.X.; writing – original draft, S.S.; writing – review & editing, H.Y., X.T., L.L., Q.W., S.S., D.M., and L.X.; funding acquisition, L.L. and L.X.; resources, H.Y. and X.T.; supervision, H.Y.; project administration, H.Y.

DECLARATION OF INTERESTS

These authors declare no competing interests.

REFERENCES

Alexandrov, A.V. (2006). Ultrasound enhanced thrombolysis for stroke. Int. J. Stroke 1, 26–29. https://doi.org/10.1111/j.1747-4949.2005.00012.x.

Armstrong, J.P.K., Puetzer, J.L., Serio, A., Guex, A.G., Kapnisi, M., Breant, A., Zong, Y., Assal, V., Skaalure, S.C., King, O., et al. (2018). Engineering anisotropic muscle tissue using acoustic cell patterning. Adv. Mater. 30, e1802649. https://doi.org/10.1002/adma.201802649.

Auffinger, B., Tobias, A.L., Han, Y., Lee, G., Guo, D., Dey, M., Lesniak, M.S., and Ahmed, A.U. (2014). Conversion of differentiated cancer cells into cancer stem-like cells in a glioblastoma model after primary chemotherapy. Cell Death Differ. 21, 1119–1131. https://doi.org/10.1038/cdd.2014.31.

Clarke, M.F., Dick, J.E., Dirks, P.B., Eaves, C.J., Jamieson, C.H., Jones, D.L., Visvader, J., Weissman, I.L., and Wahl, G.M. (2006). Cancer stem cells–perspectives on current status and future directions: AACR Workshop on cancer stem cells. Cancer Res. 66, 9339–9344. https://doi.org/10.1158/0008-5472.CAN-06-3126.

Costa, V., Carina, V., Fontana, S., De Luca, A., Monteleone, F., Pagani, S., Sartori, M., Setti, S., Faldini, C., Alessandro, R., et al. (2018). Osteogenic commitment and differentiation of human mesenchymal stem cells by low-intensity pulsed ultrasound stimulation. J. Cell Physiol. 233, 1558–1573. https://doi.org/10.1002/jcp.26058.

Daijima, Y., and Komatsu, T. (2014). Haemoglobin wrapped covalently by human serum albumin mutants containing Mn(III) protoporphyrin IX: an O2 complex stable in H2O2 solution. Chem. Commun. 50, 14716–14719. https://doi.org/10.1039/c4cc06076h.

Dezhkunov, N.V., Francescutto, A., Ciuti, P., Mason, T.J., Iernetti, G., and Kulak, A.I. (2000). Enhancement of sonoluminescence emission from a multibubble cavitation zone. Ultrason. Sonochem. 7, 19–24. https://doi.org/10.1016/s1350-4177(99)00023-1.

Dezhkunov, N.V., Francescutto, A., Serpe, L., Canaparo, R., and Cravotto, G. (2018). Sonoluminescence and acoustic emission spectra at different stages of cavitation zone development. Ultrason. Sonochem. 40, 104–109. https://doi.org/10.1016/j.ultsonch.2017.04.004.

Fouquerel, E., Barnes, R.P., Uttam, S., Watkins, S.C., Bruchez, M.P., and Opresko, P.L. (2019). Targeted and persistent 8-oxoguanine base damage at telomeres promotes telomere loss and crisis. Mol. Cell 75, 117–130.e6. https://doi.org/10.1016/j.molcel.2019.04.024.

Garofano, L., Migliozzi, S., Oh, Y.T., D'Angelo, F., Najac, R.D., Ko, A., Frangaj, B., Caruso, F.P., Yu, K., Yuan, J., et al. (2021). Pathway-based classification of glioblastoma uncovers a mitochondrial subtype with therapeutic vulnerabilities. Nat. Cancer 2, 141–156. https://doi.org/10.1038/s43018-020-00159-4.

Guzman, M.L., Rossi, R.M., Karnischky, L., Li, X., Peterson, D.R., Howard, D.S., and Jordan, C.T. (2005). The sesquiterpene lactone parthenolide induces apoptosis of human acute myelogenous leukemia stem and progenitor cells. Blood 105, 4163–4169. https://doi.org/10.1182/blood-2004-10-4135.

Han, B., Meng, X., Wu, P., Li, Z., Li, S., Zhang, Y., Zha, C., Ye, Q., Jiang, C., Cai, J., et al. (2020). ATRX/EZH2 complex epigenetically regulates FADD/PARP1 axis, contributing to TMZ resistance in glioma. Theranostics 10, 3351–3365. https://doi.org/10.7150/thno.41219.

Harrison, A., Lin, S., Pounder, N., and Mikuni-Takagaki, Y. (2016). Mode & mechanism of low intensity pulsed ultrasound (LIPUS) in fracture repair. Ultrasonics 70, 45–52. https://doi.org/10.1016/j.ultras.2016.03.016.

Hu, Y., Zhang, M., Tian, N., Li, D., Wu, F., Hu, P., Wang, Z., Wang, L., Hao, W., Kang, J., et al. (2019). The antibiotic clofoctol suppresses glioma stem cell proliferation by activating KLF13. J. Clin. Invest. 129, 3072–3085. https://doi.org/10.1172/JCI124979.

Ishiguro, T., Ohata, H., Sato, A., Yamawaki, K., Enomoto, T., and Okamoto, K. (2017). Tumor-derived spheroids: relevance to cancer stem cells and clinical applications. Cancer Sci. 108, 283–289. https://doi.org/10.1111/cas.13155.

Laprade, H., Querido, E., Smith, M.J., Guerit, D., Crimmins, H., Conomos, D., Pourret, E., Chartrand, P., and Sfeir, A. (2020). Single-molecule imaging of telomerase RNA reveals a recruitment-retention model for telomere elongation. Mol. Cell 79, 115–126.e6. https://doi.org/10.1016/j.molcel.2020.05.005.

Li, J., Liao, T., Liu, H., Yuan, H., Ouyang, T., Wang, J., Chai, S., Li, J., Chen, J., Li, X., et al. (2021). Hypoxic glioma stem cell-derived exosomes containing Linc01060 promote progression of glioma by regulating the MZF1/c-myc/HIF1alpha Axis. Cancer Res. 81, 114–128. https://doi.org/10.1158/0008-5472.CAN-20-2270.

Li, J.H., Yue, W., Huang, Z., Chen, Z.Q., Zhan, Q., Ren, F.B., Liu, J.Y., and Fu, S.B. (2011). Calcium overload induces C6 rat glioma cell apoptosis in sonodynamic therapy. Int. J. Radiat. Biol. 87, 1061–1066. https://doi.org/10.3109/09553002.2011.584938.

Liu, J., Cao, L., Chen, J., Song, S., Lee, I.H., Quijano, C., Liu, H., Keyvanfar, K., Chen, H., Cao, L.Y., et al. (2009). Bmi1 regulates mitochondrial function and the DNA damage response pathway. Nature 459, 387–392. https://doi.org/10.1038/nature08040.

Ma, A., Chen, H., Cui, Y., Luo, Z., Liang, R., Wu, Z., Chen, Z., Yin, T., Ni, J., Zheng, M., et al. (2019). Metalloporphyrin complex-based nanosonosensitizers for deep-tissue tumor theranostics by noninvasive sonodynamic therapy. Small 15, e1804028. https://doi.org/10.1002/smll.201804028.

Matteucci, C., Balestrieri, E., Argaw-Denboba, A., and Sinibaldi-Vallebona, P. (2018). Human endogenous retroviruses role in cancer cell stemness. Semin. Cancer Biol. 53, 17–30. https://doi.org/10.1016/j.semcancer.2018.10.001.

Mayo, P.H., Copetti, R., Feller-Kopman, D., Mathis, G., Maury, E., Mongodi, S., Mojoli, F., Volpicelli, G., and Zanobetti, M. (2019). Thoracic ultrasonography: a narrative review. Intensive Care Med. 45, 1200–1211. https://doi.org/10.1007/s00134-019-05725-8.

Mendez-Bermudez, A., Giraud-Panis, M.J., Ye, J., and Gilson, E. (2020). Heterochromatin replication goes hand in hand with telomere protection. Nat. Struct. Mol. Biol. 27, 313–318. https://doi.org/10.1038/s41594-020-0400-1.

Mizuno, H., Spike, B.T., Wahl, G.M., and Levine, A.J. (2010). Inactivation of p53 in breast cancers correlates with stem cell transcriptional signatures. Proc. Natl. Acad. Sci. U S A 107, 22745–22750. https://doi.org/10.1073/pnas.1017001108.

Najafi, M., Mortezaee, K., and Majidpoor, J. (2019). Cancer stem cell (CSC) resistance drivers. Life Sci. 234, 116781. https://doi.org/10.1016/j.lfs.2019.116781.

Nechiporuk, T., Kurtz, S.E., Nikolova, O., Liu, T., Jones, C.L., D'Alessandro, A., Culp-Hill, R., d'Almeida, A., Joshi, S.K., Rosenberg, M., et al. (2019). The TP53 apoptotic network is a primary mediator of resistance to BCL2 inhibition in AML cells. Cancer Discov. 9, 910–925. https://doi.org/10.1158/2159-8290.CD-19-0125.

Ni, X.J., Wang, X.D., Zhao, Y.H., Sun, H.L., Hu, Y.M., Yao, J., and Wang, Y. (2017). The effect of low-intensity ultrasound on brain-derived neurotropic factor expression in a rat Sciatic nerve crushed injury model. Ultrasound Med. Biol. 43, 461–468. https://doi.org/10.1016/j.ultrasmedbio.2016.09.017.

Ning, G.Z., Song, W.Y., Xu, H., Zhu, R.S., Wu, Q.L., Wu, Y., Zhu, S.B., Li, J.Q., Wang, M., Qu, Z.G., et al. (2019). Bone marrow mesenchymal stem cells stimulated with low-intensity pulsed ultrasound: better choice of transplantation treatment for spinal cord injury: treatment for SCI by LIPUS-BMSCs transplantation. CNS Neurosci. Ther. 25, 496–508. https://doi.org/10.1111/cns.13071.

Nusblat, L.M., Carroll, M.J., and Roth, C.M. (2017). Crosstalk between M2 macrophages and glioma stem cells. Cell Oncol. 40, 471–482. https://doi.org/10.1007/s13402-017-0337-5.

Ostrom, Q.T., Cote, D.J., Ascha, M., Kruchko, C., and Barnholtz-Sloan, J.S. (2018). Adult glioma incidence and survival by race or ethnicity in the United States from 2000 to 2014. JAMA Oncol. *4*, 1254–1262. https://doi.org/10.1001/jamaoncol.2018.1789.

Ozer, O., Bhowmick, R., Liu, Y., and Hickson, I.D. (2018). Human cancer cells utilize mitotic DNA synthesis to resist replication stress at telomeres regardless of their telomere maintenance mechanism. Oncotarget *9*, 15836–15846. https://doi.org/10.18632/oncotarget.24745.

Ozer, O., and Hickson, I.D. (2018). Pathways for maintenance of telomeres and common fragile sites during DNA replication stress. Open Biol. *8*, 180018. https://doi.org/10.1098/rsob.180018.

Passos, J.F., Saretzki, G., and von Zglinicki, T. (2007). DNA damage in telomeres and mitochondria during cellular senescence: is there a connection? Nucleic Acids Res. *35*, 7505–7513. https://doi.org/10.1093/nar/gkm893.

Qian, W., Kumar, N., Roginskaya, V., Fouquerel, E., Opresko, P.L., Shiva, S., Watkins, S.C., Kolodieznyi, D., Bruchez, M.P., and Van Houten, B. (2019). Chemoptogenetic damage to mitochondria causes rapid telomere dysfunction. Proc. Natl. Acad. Sci. U S A *116*, 18435–18444. https://doi.org/10.1073/pnas.1910574116.

Qu, F., Wang, P., Zhang, K., Shi, Y., Li, Y., Li, C., Lu, J., Liu, Q., and Wang, X. (2020). Manipulation of Mitophagy by "All-in-One" nanosensitizer augments sonodynamic glioma therapy. Autophagy *16*, 1413–1435. https://doi.org/10.1080/15548627.2019.1687210.

Reya, T., Morrison, S.J., Clarke, M.F., and Weissman, I.L. (2001). Stem cells, cancer, and cancer stem cells. Nature *414*, 105–111. https://doi.org/10.1038/35102167.

Rudolph, K.L., Chang, S., Lee, H.W., Blasco, M., Gottlieb, G.J., Greider, C., and DePinho, R.A. (1999). Longevity, stress response, and cancer in aging telomerase-deficient mice. Cell *96*, 701–712. https://doi.org/10.1016/s0092-8674(00)80580-2.

Saravelos, S.H., Jayaprakasan, K., Ojha, K., and Li, T.C. (2017). Assessment of the uterus with three-dimensional ultrasound in women undergoing ART. Hum. Reprod. Update *23*, 188–210. https://doi.org/10.1093/humupd/dmw040.

Saygin, C., Matei, D., Majeti, R., Reizes, O., and Lathia, J.D. (2019). Targeting cancer stemness in the clinic: from hype to hope. Cell Stem Cell *24*, 25–40. https://doi.org/10.1016/j.stem.2018.11.017.

Sazgarnia, A., Shanei, A., Eshghi, H., Hassanzadeh-Khayyat, M., Esmaily, H., and

Shanei, M.M. (2013). Detection of sonoluminescence signals in a gel phantom in the presence of Protoporphyrin IX conjugated to gold nanoparticles. Ultrasonics *53*, 29–35. https://doi.org/10.1016/j.ultras.2012.03.009.

Sharanek, A., Burban, A., Laaper, M., Heckel, E., Joyal, J.S., Soleimani, V.D., and Jahani-Asl, A. (2020). OSMR controls glioma stem cell respiration and confers resistance of glioblastoma to ionizing radiation. Nat. Commun. *11*, 4116. https://doi.org/10.1038/s41467-020-17885-z.

Tarry-Adkins, J.L., Martin-Gronert, M.S., Chen, J.H., Cripps, R.L., and Ozanne, S.E. (2008). Maternal diet influences DNA damage, aortic telomere length, oxidative stress, and antioxidant defense capacity in rats. FASEB J. *22*, 2037–2044. https://doi.org/10.1096/fj.07-099523.

Ting, C.Y., Fan, C.H., Liu, H.L., Huang, C.Y., Hsieh, H.Y., Yen, T.C., Wei, K.C., and Yeh, C.K. (2012). Concurrent blood-brain barrier opening and local drug delivery using drug-carrying microbubbles and focused ultrasound for brain glioma treatment. Biomaterials *33*, 704–712. https://doi.org/10.1016/j.biomaterials.2011.09.096.

Trendowski, M., Wong, V., Zoino, J.N., Christen, T.D., Gadeberg, L., Sansky, M., and Fondy, T.P. (2015). Preferential enlargement of leukemia cells using cytoskeletal-directed agents and cell cycle growth control parameters to induce sensitivity to low frequency ultrasound. Cancer Lett. *360*, 160–170. https://doi.org/10.1016/j.canlet.2015.02.001.

Varela, E., Munoz-Lorente, M.A., Tejera, A.M., Ortega, S., and Blasco, M.A. (2016). Generation of mice with longer and better preserved telomeres in the absence of genetic manipulations. Nat. Commun. *7*, 11739. https://doi.org/10.1038/ncomms11739.

Viani, L., Corbella, M., Curutchet, C., O'Reilly, E.J., Olaya-Castro, A., and Mennucci, B. (2014). Molecular basis of the exciton-phonon interactions in the PE545 light-harvesting complex. Phys. Chem. Chem. Phys. *16*, 16302–16311. https://doi.org/10.1039/c4cp01477d.

Vousden, K.H., and Lane, D.P. (2007). p53 in health and disease. Nat. Rev. Mol. Cell Biol. *8*, 275–283. https://doi.org/10.1038/nrm2147.

Wan, Q., Zou, C., Hu, D., Zhou, J., Chen, M., Tie, C., Qiao, Y., Yan, F., Cheng, C., Sheng, Z., et al. (2019). Imaging-guided focused ultrasound-induced thermal and sonodynamic effects of nanosonosensitizers for synergistic enhancement of glioblastoma therapy. Biomater. Sci. *7*, 3007–3015. https://doi.org/10.1039/c9bm00292h.

Wang, X., Jia, Y., Wang, P., Liu, Q., and Zheng, H. (2017). Current status and future perspectives of sonodynamic therapy in glioma treatment. Ultrason. Sonochem. *37*, 592–599. https://doi.org/10.1016/j.ultsonch.2017.02.020.

Wang, X., Prager, B.C., Wu, Q., Kim, L.J.Y., Gimple, R.C., Shi, Y., Yang, K., Morton, A.R., Zhou, W., Zhu, Z., et al. (2018). Reciprocal signaling between glioblastoma stem cells and differentiated tumor cells promotes malignant progression. Cell Stem Cell *22*, 514–528.e5. https://doi.org/10.1016/j.stem.2018.03.011.

Wei, S., Qiu, T., Yao, X., Wang, N., Jiang, L., Jia, X., Tao, Y., Wang, Z., Pei, P., Zhang, J., et al. (2020). Arsenic induces pancreatic dysfunction and ferroptosis via mitochondrial ROS-autophagy-lysosomal pathway. J. Hazard Mater. *384*, 121390. https://doi.org/10.1016/j.jhazmat.2019.121390.

Weller, M., Wick, W., Aldape, K., Brada, M., Berger, M., Pfister, S.M., Nishikawa, R., Rosenthal, M., Wen, P.Y., Stupp, R., et al. (2015). Glioma. Nat. Rev. Dis. Primers *1*, 15017. https://doi.org/10.1038/nrdp.2015.17.

Wu, P., Dong, W., Guo, X., Qiao, X., Guo, S., Zhang, L., Wan, M., and Zong, Y. (2019). ROS-responsive blended nanoparticles: cascade-amplifying synergistic effects of Sonochemotherapy with on-demand boosted drug release during SDT process. Adv. Healthc. Mater. *8*, e1900720. https://doi.org/10.1002/adhm.201900720.

Xu, Z.Y., Li, X.Q., Chen, S., Cheng, Y., Deng, J.M., and Wang, Z.G. (2012). Glioma stem-like cells are less susceptible than glioma cells to sonodynamic therapy with photofrin. Technol. Cancer Res. Treat. *11*, 615–623. https://doi.org/10.7785/tcrt.2012.500277.

Yu, S.C., Ping, Y.F., Yi, L., Zhou, Z.H., Chen, J.H., Yao, X.H., Gao, L., Wang, J.M., and Bian, X.W. (2008). Isolation and characterization of cancer stem cells from a human glioblastoma cell line U87. Cancer Lett. *265*, 124–134. https://doi.org/10.1016/j.canlet.2008.02.010.

Zhang, H., Chen, J., Zhu, X., Ren, Y., Cao, F., Zhu, L., Hou, L., Zhang, H., and Zhang, Z. (2018). Ultrasound induced phase-transition and invisible nanobomb for imaging-guided tumor sonodynamic therapy. J. Mater. Chem. B *6*, 6108–6121. https://doi.org/10.1039/c8tb01788c.

Zhou, B.B., Zhang, H., Damelin, M., Geles, K.G., Grindley, J.C., and Dirks, P.B. (2009). Tumour-initiating cells: challenges and opportunities for anticancer drug discovery. Nat. Rev. Drug Discov. *8*, 806–823. https://doi.org/10.1038/nrd2137.

STAR★METHODS

KEY RESOURCES TABLE

REAGENT or RESOURCE	SOURCE	IDENTIFIER
Antibodies		
BD Pharmingen™ PE mouse anti-human CD133	BD Pharmingen	Cat #566594 RRID: AB_2744281
BD Pharmingen™Alexa Fluor® 647 mouse anti-nestin	BD Pharmingen	Cat #560393 RRID: AB_1645170
FITC anti-BrdU flow kit	BD Pharmingen	Cat # 559619 RRID: AB_2617060
APC Annexin V	BD Pharmingen	Cat #550475 RRID: AB_2868885
Recombinant Anti-CD133 antibody	Abcam	ab216323 RRID: AB_2847920
Anti-estin antibody	Abcam	ab18102 RRID: AB_444246
Recombinant Anti-Ki67 antibody	Abcam	ab279653 RRID: AB_302459
Fluorescein (FITC)–conjugated Affinipure goat anti-mouse IgG(H + L)	Proteintech	SA00003-1 RRID: AB_2890896
CoraLite594 – conjugated goat anti-rabbit IgG(H + L)	Proteintech	RRID: AB_2810984
53BP1 antibody	Novus Biologicals	NB100-304
GLI1 (V812) antibody	Cell Signaling Technology	#2534 RRID: AB_2294745
PTCH1 (C53A3) rabbit mAb	Cell Signaling Technology	#2468 RRID: AB_2300741
Wnt3a (C64F2) rabbit mAb	Cell Signaling Technology	#2721 RRID: AB_2215411
Wnt5a/b (C27 × 10^8) rabbit mAb	Cell Signaling Technology	#2530 RRID: AB_2215595
β-Catenin (D10A8) XP® Rabbit mAb	Cell Signaling Technology	#8480 RRID: AB_11127855
PLK1 (208G4) rabbit mAb	Cell Signaling Technology	#4513 RRID: AB_2167409
cdc2 (POH1) mouse mAb	Cell Signaling Technology	#9116 RRID: AB_2074795
Cyclin B1 (D5C10) XP® Rabbit mAb	Cell Signaling Technology	#12231 RRID: AB_2783553
GAPDH (D16H11) XP® Rabbit mAb	Cell Signaling Technology	#5174 RRID: AB_10622025
Anti-mouse IgG, HRP-linked Antibody	Cell Signaling Technology	#7076 RRID: AB_330924
Anti-rabbit IgG, HRP-linked antibody	Cell Signaling Technology	#7074 RRID: AB_2099233
Chemicals, peptides, and recombinant proteins		
CCk-8 kit	ZETA	No.: k009
TRIzol™ LS reagent	Invitrogen	Lot 264006
RT-PCR kit	Abgen biotechnology	06-104
ChamQ Universal SYBR qPCR master mix	Vazyme Biotech	Q711-02
RIPA buffer(high)	Solarbio	R0010
DNA extraction kit	Biogama	BW-GD2211-01
Colchicine solution	Biological Industries	1952210
JC-1 detection kit	Dojindo Molecular Technology	MT09
Singlet oxygen detection kit	Bestbio	BB-47055
Singlet oxygen detection kit	Invitrogen	S36002
7-ADD	BD Pharmingen	Cat # 559925 RRID: AB_2869266
TelC-FITC PNA probe	Panagene	F1009
Recombinant human yt c	Novoprotein	No.:CF80
Recombinant humanCyt c1	Abnova	Cat#H00001537-p02

(Continued on next page)

Continued

REAGENT or RESOURCE	SOURCE	IDENTIFIER
Recombinant human CYB5A(N-6His)	Novoprotein	#C217
Recombinant human CYB5B(C-6His)	Novoprotein	#CJ36
N-2 Supplement (100X)	Gibco	2245840
B-27 Supplement (50X)	Gibco	2234290
Recombinant human EGF	PerproTech	AF-100-15
Recombinant human FGF basic	PerproTech	100-18B
Temozolomide	Sigma	T2577
Mito-TEMPO	GLPBIO	GC31682
Colorimetric TUNEL apoptosis assay kit	Beyotime	C1098
MEM (1X)	Gibco	11095080
DMEM basic (1X)	Gibco	C11995500BT
DMEM/F-12 (1:1) basic (1X)	Gibco	C11330500BT
Experimental models: cell lines		
U87MG	BNCC	BNCC100646
A172	iCell Bioscience Inc	N/A
TBD0220	Tianjin Medical University General Hospital	N/A
Experimental models: organisms/strains		
Mouse: BALB-c nude mice	the Experimental Animal Center of Academy of Military Medical Sciences, China	N/A

RESOURCE AVAILABILITY

Lead contact

Further information and requests for resources and reagents should be directed to and will be fulfilled by the lead contact, Hua Yan (yanhua20042007@sina.com).

Materials availability

This study did not generate new unique reagents.

Data and code availability

The raw data involved in the manuscript have been deposited at Mendeley Data and is publicly available as of the date of publication. Mendeley Data, https://doi.org/10.17632/r94wfc8xvd.1.

This paper does not report original code.

Any additional information required to reanalyze the data reported in this paper is available from the lead contact upon request.

EXPERIMENTAL MODEL AND SUBJECT DETAILS

Cell culture and dedifferentiation

Glioblastoma cells U87MG was sourced from BNCC and A172 were sourced from iCell Bioscience Inc. TBD0220 cell (TBD) is a primary cell line, which were provided by Professor Chunsheng Kang of Tianjin Medical University General Hospital. U87MG cells were maintained in MEM, A172 cells were maintained in DMEM and TBD cells were maintained in DMEM/F12 and cultured continuously at 37°C in a humidified chamber at 5% CO_2 with 10% fetal bovine serum and 1% penicillin/streptomycin (Thermo Fisher, USA). Gi-loma cells were made into single cell suspensions by trypsin, washed twice with DMEM/F12 and then were cultured in stem cell medium containing DMEM/F12, N2, B27, epidermal growth factor, and basic fibro-blast growth factor . Glioma cells become rounded and non-adherent and start to form glioma stem cell (GSC) spheres. GSCs were treated with trypsin for 70 seconds, washed twice with DMEM/F12 and then

were cultured in stem cell medium. This procedure was repeated every 2days for 7 to 9 days. At this point, a mass of GSC spheres was visible under microscopy (Figure S1).

Tumor xenograft study

All experimental protocols were conducted in accordance with national legislation and associated guidelines. BALB-c nude mice (male; grade SPF; 4–6 w, 16–18 g) were purchased from the Experimental Animal Center of Academy of Military Medical Sciences, China. The xenograft tumor volume was calculated according to the formula V = $1/6\pi$ (ab^2), and then the tumor growth curves were plotted.

LIPUS stimulating

LIPUS is sinusoidal ultrasound with a frequency of 1.5 MHz. The specific setup of the ultrasound treatment (Figure S2) is: ultrasound device (2776 Intelect Mobile US, DJO GLOBAL Chattanooga Co., Ltd. USA) using a planar ultrasound transducer (5 cm^2). As shown in Figure S2, cells were sonicated at 300 MW/cm^2 and the 1.0 kHz system with the duty ratio of 0.2 (200 ms pulses of ultrasound with 800 ms between each pulse). LIPUS was performed every day for 20 min for 24, 48, and 72 h. For nude mice, LIPUS was performed every three days for 5 min.

Ethics statement. All animal studies were approved by the Ethics Committee of Tianjin Huanhu Hospital.

METHOD DETAILS

Immunofluorescence staining

GSCs were plated onto poly-L-lysine-coated glass coverslips in DMEM/F12 for 1 h, washed three times with PBS and then fixed with 4% paraformaldehyde (Sigma, USA) for 20 min. Then, the cells were incubated with antibodies against CD133 and Nestin at 4°C overnight, washed with PBS and incubated with secondary antibodies at 37°C for 1 h. The nuclei were stained with DAPI. The slides were examined using confocal microscopy.

CCK-8 assay

CCK-8 assays were applied to analyze the influence of LIPUS on the proliferation of GSCs. The cells were plated at a density of 1 × 10^6 per 96-well plate. Next, 10 μL of CCK-8 solution was added to each well for 1–4 h at 37°C, and the absorbance was measured at 450 nm using a microplate reader (Molecular Devices).

Annexin V/7-AAD apoptosis assay

Annexin V/7-AAD apoptosis assays were applied to analyze the influence of LIPUS on the apoptosis of the GSCs. The cells were harvested and suspended in 100 μL of binding buffer (0.1 M HEPES at pH 7.4, 1.4 M NaCl, 25 mM $CaCl_2$) at a density of 1 × 10^6 cells/mL. The cell suspension was mixed with APC-Annexin V and 7-ADD and incubated in a dark chamber for 15 min. Apoptotic cells were detected and calculated using a BD Caliber flow cytometer. The total percentage of Annexin V-positive cells was calculated quantitatively.

5-Bromodeoxyuridine (BrdU)

BrdU assays were applied to analyze the influence of LIPUS on the cell cycle of the GSCs. The cells were plated at a density of 2 × 10^6 per 6-well plate. BrdU was added to the cell suspensions and cultured at 37°C for 1 h. After fixed, permeabilized and treated by DNase for 1 h at 37°C, the cells were stained with FITC-anti-BrdU and 7-AAD for 20 min respectively. Then the cells were analyzed using a BD Caliber flow cytometer.

Fluorescence-activated cell sorting (FACS)

GSCs were collected and resuspended in 100 μL antibody incubation buffer. Anti-CD133 antibody was added and incubated on ice for 30 min. After centrifugation and resuspension, the cells were fixed and membrane-perforated. Then, 20 μL anti-Nestin antibody was added. The expression rates were detected and calculated using a BD Caliber flow cytometer.

qPCR (quantitative PCR) and RT-PCR (reverse Transcription-PCR)

Genomic DNA was collected by DNA extraction kit and total RNA was extracted using TRIzol. RNA was reverse transcribed by RT-PCR kits. qPCR was performed on a Roche Lightcycler II using target gene and the reference control gene primers. The qPCR primers are presented in Table S1.

Metaphase spreads and telomere fluorescence in situ hybridization (FISH) analysis

FISH was used to detect the telomere loss. GSCs were collected and treated with 10 μg/mL colcemid for 20 h, incubated with 75 mM KCl for half an hour at 37°C, prefixed for 5 min and then fixed for 1 h with a mixture of methanol and glacial acetic acid (3:1). The cells were dropped onto water-coated slides to spread the metaphase chromosomes. Then, the slides were stained with the PNA probe following the manufacturer's protocol. Images were captured by a Nikon Ti inverted fluorescence microscope. The images were analyzed using NIS Elements Advanced Research software.

Immunofluorescence and telomere fluorescence *in situ* hybridization (IF-FISH)

Telomere damage was analyzed with IF-FISH. GSCs were plated onto poly-L-lysine-coated glass coverslips in DMEM/F12 for 1 h and then fixed with 4% paraformaldehyde for 20 min. The cells were permeabilized with 0.2% Triton X-100 (Sigma, USA) and dehydrated through graded alcohol. The coverslips were hybridized with the PNA probe, 53 bp1 antibody and secondary antibody following the manufacturer's protocol. Images were acquired on a Nikon Ti inverted fluorescence microscope. The images were deconvoluted and analyzed using NIS Elements Advance research software. The foci counts were exported to Excel for analysis.

Western blotting

Proteins were extracted from GSCs treated with LIPUS using RIPA lysis buffer and PMSF (Solarbio Co., Beijing, China) following the manufacturer's protocols. The proteins were separated by SDS-PAGE, transferred to a nitrocellulose membrane, blocked with bovine serum albumin and then incubated with primary antibodies against Gli1, PTCH, Wnt3, Wnt5a, β-catenin, PLK1, CDK1, Cyclin B and GAPDH (CST, USA) at 4°C overnight. After the membrane was incubated with the goat anti-rabbit/mouse IgG HRP secondary antibody (CST, USA) for 90 min, chemiluminescence membrane exposure and enhancement were performed.

Mitochondrial membrane potential assay

A mitochondrial membrane potential assay was performed with a JC-1 detection kit. The GSCs were collected and resuspended in 1 mol/L JC-1 probe and incubated at 37°C and 5% CO_2 for 1 h protected from light. After washing with PBS twice, the cells were immediately photographed under a confocal microscope, and the fluorescence intensity was measured by a microplate reader.

Singlet oxygen ($^1O_2$) detection

Singlet oxygen fluorescence intensity was detected by the enzyme labeler, and GSCs were photographed under a confocal microscope following the manufacturer's instructions. GSCs were collected and resuspended in 10 μL $^1O_2$ probe and incubated at 37°C and 5% CO_2 for 1 h protected from light. After washing with PBS twice, the cells were immediately photographed under a confocal microscope, and the fluorescence intensity was measured by a microplate reader.

Ten microliters of cyt B5A, cyt B5B, cyt C, cyt C1, and ddH_2O were individually added to each 384-well plate, with 3 repeated wells in every group, named the cyt B5A group, cyt B5B group, cyt C group, cyt C1 group, and control group. Next, 20 μL of $^1O_2$ probe was added and mixed into every well 5 min before LIPUS stimulation. Once the stimulation was over, the samples were immediately tested by a fluorescence marker.

Immunohistochemistry

TdT-mediated dUTP nick end labeling (TUNEL) and Ki67 staining at the end of the 16-day experimental period were used to analyze the apoptosis and proliferation of the tumor tissues. The tumor tissue was removed, fixed in 4% paraformaldehyde for 24 h, and then embedded in paraffin for preservation. Paraffin sections were dewaxed with xylene, dehydrated with gradient alcohol, subjected to antigen retrieval, blocked and then incubated with antibodies against Ki67 overnight. After the appropriate specific

secondary antibody was added, the staining results were observed under a microscope after the color development of DAB.

Paraffin sections were dewaxed with xylene, dehydrated with gradient alcohol and washed with PBS. Proteinase K buffer (Sigma, USA) was added for 30 min. After washing with PBS, 50 μL TUNEL reaction mixture (5 μL TdT+45 μL fluorescein labeled dUTP solution) was added, and the slides were placed in a humidified box at 37° in the dark for 1 h. The slides were washed with PBS and incubated with DAPI for 5 min. Then, the slices were sealed and observed under a fluorescence microscope.

QUANTIFICATION AND STATISTICAL ANALYSIS

Statistical analyses were performed using SPSS scientific software. The applied methods were Student's t-test for the comparison of two groups and one-way ANOVA for more than two comparisons. Differences with p values less than 0.05 were considered statistically significant. Data are Means $\pm$ SD, $*p < 0.05$, $**p < 0.01$, $***p < 0.001$.